

An Air-Stable and Li-Metal-Compatible Glass-Ceramic Electrolyte enabling High-Performance All-Solid-State Li Metal Batteries

Feipeng Zhao, Sandamini H. Alahakoon, Keegan Adair, Shumin Zhang, Wei Xia, Weihan Li, Chuang Yu, Renfei Feng, Yongfeng Hu, Jianwen Liang, Xiaoting Lin, Yang Zhao, Xiaofei Yang, Tsun-Kong Sham, Huan Huang, Li Zhang, Shangqian Zhao, Shigang Lu, Yining Huang,* and Xueliang Sun*


The development of all-solid-state Li metal batteries (ASSLMBs) has attracted significant attention due to their potential to maximize energy density and improved safety compared to the conventional liquid-electrolyte-based Li-ion batteries. However, it is very challenging to fabricate an ideal solid-state electrolyte (SSE) that simultaneously possesses high ionic conductivity, excellent air-stability, and good Li metal compatibility. Herein, a new glass-ceramic $\text{Li}_{3.2}\text{P}_{0.8}\text{Sn}_{0.2}\text{S}_4$ (gc- $\text{Li}_{3.2}\text{P}_{0.8}\text{Sn}_{0.2}\text{S}_4$) SSE is synthesized to satisfy the aforementioned requirements, enabling high-performance ASSLMBs at room temperature (RT). Compared with the conventional Li_3PS_4 glass-ceramics, the present gc- $\text{Li}_{3.2}\text{P}_{0.8}\text{Sn}_{0.2}\text{S}_4$ SSE with 12% amorphous content has an enlarged unit cell and a high Li^+ ion concentration, which leads to 6.2-times higher ionic conductivity ($1.21 \times 10^{-3} \text{ S cm}^{-1}$ at RT) after a simple cold sintering process. The (P/Sn) S_4 tetrahedron inside the gc- $\text{Li}_{3.2}\text{P}_{0.8}\text{Sn}_{0.2}\text{S}_4$ SSE is verified to show a strong resistance toward reaction with H_2O in 5%-humidity air, demonstrating excellent air-stability. Moreover, the gc- $\text{Li}_{3.2}\text{P}_{0.8}\text{Sn}_{0.2}\text{S}_4$ SSE triggers the formation of Li–Sn alloys at the Li/SSE interface, serving as an essential component to stabilize the interface and deliver good electrochemical performance in both symmetric and full cells. The discovery of this gc- $\text{Li}_{3.2}\text{P}_{0.8}\text{Sn}_{0.2}\text{S}_4$ superionic conductor enriches the choice of advanced SSEs and accelerates the commercialization of ASSLMBs.

All-solid-state lithium metal batteries (ASSLMBs) have been regarded as ideal energy storage devices because of their potential to maximize energy density and improve safety.^[1–3] As a key part of ASSLMBs, the development of solid-state electrolytes (SSEs) has drawn increasing attention.^[4,5] Among the various types of SSEs, the inorganic glass-ceramic SSE is one of the most promising categories.^[6,7] Apart from the advantages of high ionic conductivity and superior mechanical properties in comparison to organic polymer-based SSEs, the glass-ceramic SSEs also show minimal grain boundary resistance and good contact with electrode materials compared to other inorganic ceramic SSEs.^[8,9]

Sulfide-based glass-ceramic SSEs have received great attention due to their relatively low glass transition temperature (T_g , lower than 300 °C).^[6,10] The metastable Li-ion conductors (e.g., $\beta\text{-Li}_3\text{PS}_4$ and $\text{Li}_7\text{P}_3\text{S}_{11}$) can be precipitated from glass precursors and stabilized in a glass

F. Zhao, K. Adair, S. Zhang, Dr. W. Xia, Dr. W. Li, Dr. C. Yu, Dr. J. Liang, Dr. X. Lin, Dr. Y. Zhao, Dr. X. Yang, Prof. X. Sun
Department of Mechanical and Materials Engineering
University of Western Ontario
London, Ontario N6A 5B9, Canada
E-mail: xsun9@uwo.ca

S. H. Alahakoon, S. Zhang, Prof. T.-K. Sham, Prof. Y. Huang
Department of Chemistry
University of Western Ontario
London, Ontario N6A 5B7, Canada
E-mail: yhuang@uwo.ca

 The ORCID identification number(s) for the author(s) of this article can be found under <https://doi.org/10.1002/adma.202006577>.

DOI: 10.1002/adma.202006577

Dr. W. Xia
Academy for Advanced Interdisciplinary Studies
Southern University of Sciences and Technology
1088 Xueyuan Avenue, Shenzhen 518000, P. R. China

Dr. R. Feng, Y. Hu
Canadian Light Source Inc.
University of Saskatchewan
Saskatoon, Saskatchewan S7N 2V3, Canada

Dr. H. Huang
Glabat Solid-State Battery Inc.
700 Collip Circle, London, Ontario N6G 4X8, Canada

Dr. L. Zhang, Dr. S. Zhao, Dr. S. Lu
China Automotive Battery Research Institute Co., Ltd.
No. 11 Xingke East Street, Yanqi Economic Development Area
Huairou District, Beijing 101407, P. R. China

matrix at room temperature (RT).^[11–13] Therefore, sulfide-based glass-ceramic SSEs are able to possess high ionic conductivities that are comparable to the well-known crystallized Li argyrodites or thiophosphate SSEs.^[6,14] However, sulfide-based glass-ceramic SSEs suffer from poor air-stability and Li metal incompatibility,^[15] due to the facts that 1) Sulfide-based SSEs are constructed from P-centered polyhedral units and are extremely hygroscopic because of the intimate affinity between P and O from the moisture. Moreover, the S ligands tend to combine with H and generate toxic H₂S gas.^[16] It is noted that Li₃PS₄-based sulfide SSEs shows relatively better resistance toward moisture among the various Li₂S-P₂S₅ electrolyte systems.^[16] 2) Sulfide-based SSEs are prone to (electro)chemical reduction from the Li metal anode.^[17] There is also a possibility that uneven Li deposition occurs at the Li/sulfide interface, leading to the formation of Li dendrites which may penetrate the soft electrolyte layer and cause short-circuits.^[18] Therefore, it is rarely reported that a sulfide electrolyte can be used directly (without interlayers) facing Li metal to construct a workable ASSLMB.^[6,19]

To increase the air-stability of sulfide-based SSEs, crystallized Li₂SnS₃ and Li₄SnS₄ SSEs were developed.^[20,21] Based on the hard and soft acids and bases (HSAB) theory, the Sn prefers to bond with S rather than interact with O when exposed to air. However, the limited ionic conductivity ($\approx 10^{-5}$ S cm⁻¹) at RT hinders their applications.^[21,22] Although Arsenic (As)-substituted Li₄SnS₄ SSEs can increase the ionic conductivity to 10⁻³ S cm⁻¹ at RT, the hyper toxic As-based compounds prevent their commercialization.^[22] Very recently, fractional substitution of P with Sn, Sb, or Zn in the crystallized sulfide SSEs have been reported to improve the air-stability,^[23–26] but either insufficient ionic conductivity or poor compatibility with Li metal has impeded them to be used as a single-layer electrolyte for applications. To improve the Li metal compatibility, in addition to the additional and complicated interfacial modification (i.e., pre-treatment of Li metal and utilization of interlayers),^[27–30] synthesizing sulfide SSEs with introducing halide elements has been verified as a more effective strategy that can increase the exchange current density and reduce the manufacturing cost.^[31,32] Despite the progress, it is still very difficult to overcome the challenges of using the modified SSEs as a monolayer to fabricate practical ASSLMBs, which requires good ionic conductivity ($>10^{-3}$ S cm⁻¹), air-stability, as well as Li metal compatibility in an integrated manner.^[2,3]

Herein, via selective Sn-substitution in the P sites of one classic glass-ceramic β -Li₃PS₄ (gc-Li₃PS₄), a new glass-ceramic Li_{3.2}P_{0.8}Sn_{0.2}S₄ (gc-Li_{3.2}P_{0.8}Sn_{0.2}S₄) SSE is obtained that can satisfy all the requirements to enable high-performance ASSLMBs. Our gc-Li_{3.2}P_{0.8}Sn_{0.2}S₄ SSEs possess an enlarged lattice and higher Li⁺ ion concentration compared with gc-Li₃PS₄, offering a 6.2-fold increase in ionic conductivity (1.21×10^{-3} S cm⁻¹) at RT. ³¹P magic-angle spinning (MAS) solid-state nuclear magnetic resonance (SS-NMR) spectroscopy was used, for the first time, to estimate the amount of amorphous material in the glass-ceramic SSEs. Benefiting from the strong affinity of Sn toward S, the new electrolyte shows excellent air-stability, which paves the way for large-scale processing in conventional dry rooms. Moreover, the incorporated Sn in the electrolyte is found to be capable of forming a Li–Sn alloy at the interface

between the electrolyte and Li metal anode. This interface can enable smooth Li deposition and provides highly reversible cycling in all cell formats.

The gc-Li_{3.2}P_{0.8}Sn_{0.2}S₄ SSEs were prepared via a two-step solid-state reaction method. Ball-milling was firstly used to make the stoichiometric precursor fully amorphous. Subsequently, the glass-state precursor was converted to a glass-ceramic state after a specific annealing process (see the Experimental Section in the Supporting Information for details). Synchrotron-based X-ray diffraction (SXRD) patterns of the electrolytes at different stages of synthesis are shown in **Figure 1a**. The featureless patterns of the electrolytes obtained after the first step indicate the success of amorphization for the precursors, namely glass-state Li_{3.2}P_{0.8}Sn_{0.2}S₄ (g-Li_{3.2}P_{0.8}Sn_{0.2}S₄). Differential scanning calorimeter (DSC) analysis of the g-Li_{3.2}P_{0.8}Sn_{0.2}S₄ revealed that ≈ 259 °C is the T_g of the Li_{3.2}P_{0.8}Sn_{0.2}S₄ phase, which is higher than that of β -Li₃PS₄ (Figure S1, Supporting Information). After annealing g-Li_{3.2}P_{0.8}Sn_{0.2}S₄ at 260 °C for 4 h, the gc-Li_{3.2}P_{0.8}Sn_{0.2}S₄ SSE was obtained. The characteristic diffraction peaks of gc-Li_{3.2}P_{0.8}Sn_{0.2}S₄ SSE are nearly identical to those of the gc-Li₃PS₄ SSEs, belonging to the metastable β -phase (PDF Card No. 04-010-1784). Nevertheless, upon close observation of the SXRD patterns (Figure S2, Supporting Information), there is a low-angle shift occurring in the gc-Li_{3.2}P_{0.8}Sn_{0.2}S₄ sample, suggesting an expansion of the crystal structure after incorporating Sn ($R_{\text{Sn}^{4+}}$: 0.55 Å > $R_{\text{P}^{5+}}$: 0.17 Å). The 2D diffraction patterns of g-Li_{3.2}P_{0.8}Sn_{0.2}S₄ and gc-Li_{3.2}P_{0.8}Sn_{0.2}S₄ SSEs were recorded on the detector as displayed in Figure 1b,c, respectively. The distinct diffraction rings for the gc-Li_{3.2}P_{0.8}Sn_{0.2}S₄ SSE suggest the crystallinity is improved significantly after annealing. Raman measurements confirm that the incorporated Sn can partially replace P and bonds with S in the gc-Li_{3.2}P_{0.8}Sn_{0.2}S₄ SSEs. As shown in Figure 1d, the featured peaks at 345.4 and 419.6 cm⁻¹ in the gc-Li_{3.2}P_{0.8}Sn_{0.2}S₄ sample can be ascribed to the stretching vibrations of Sn–S and P–S in forms of SnS₄ and PS₄ tetrahedrons, respectively.^[33,34] X-ray absorption near edge spectroscopies (XANES) of P and S K-edges proves that the incorporated Sn affect the fine structure of P and S atoms in the tetrahedra (Figure S3, Supporting Information). Furthermore, scanning electron microscope (SEM) imaging combined with energy dispersive spectroscopy (EDS) elemental mapping indicates that P, S, and Sn are homogeneously dispersed in the sub-micro and irregular gc-Li_{3.2}P_{0.8}Sn_{0.2}S₄ particles (Figure S4, Supporting Information). The conformal distribution of Sn reflects that Sn is incorporated into the gc-Li_{3.2}P_{0.8}Sn_{0.2}S₄ rather than being present as part of a physical mixture.

Rietveld refinement of the low-speed-scan XRD (Bruker) pattern of gc-Li_{3.2}P_{0.8}Sn_{0.2}S₄ reveals the crystal information of the Li_{3.2}P_{0.8}Sn_{0.2}S₄ phase (Figure 1e). This composition is the only observed crystalline phase, which is analogous to the β -Li₃PS₄, belonging to the orthorhombic space group. The unit cell parameters of the Li-rich Li_{3.2}P_{0.8}Sn_{0.2}S₄ ($a = 13.159$ Å, $b = 8.025$ Å, $c = 6.135$ Å) are consistently larger than those of β -Li₃PS₄ ($a = 13.066$ Å, $b = 8.015$ Å, $c = 6.101$ Å) (Tables S1 and S2, Supporting Information). This result quantifies the influence of Sn incorporation on the crystallographic structure, and further elucidates the reason for the low-angle shift of the diffraction peaks. The Rietveld analysis also suggests that the incorporated Sn atoms share the 4c site with P atoms and present an

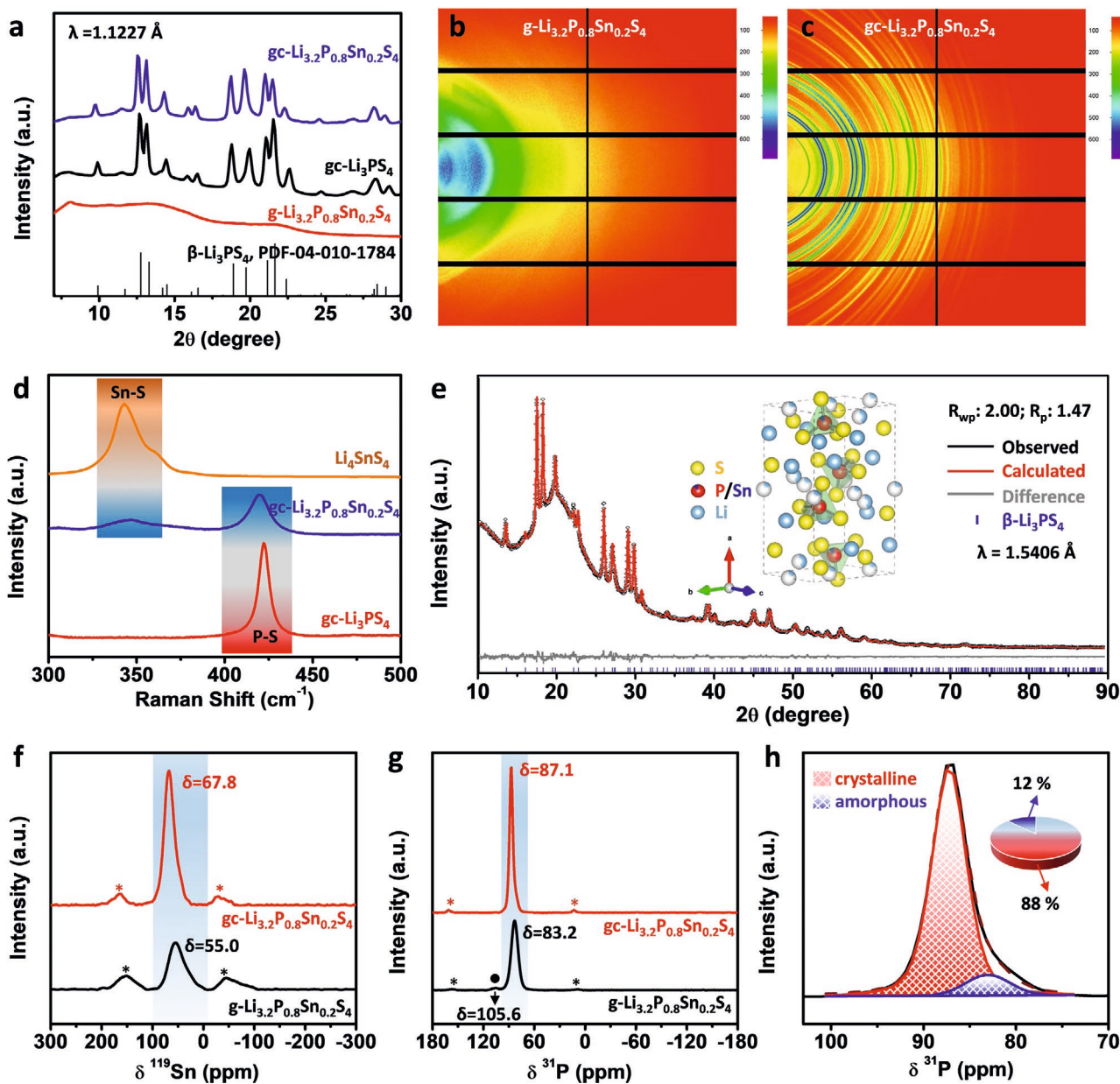


Figure 1. Structural analysis of $gc\text{-Li}_{3.2}\text{P}_{0.8}\text{Sn}_{0.2}\text{S}_4$ SSEs. a) SXRD patterns of $gc\text{-Li}_{3.2}\text{P}_{0.8}\text{Sn}_{0.2}\text{S}_4$ SSEs compared with $gc\text{-Li}_{3.2}\text{P}_{0.8}\text{Sn}_{0.2}\text{S}_4$ and $gc\text{-Li}_3\text{PS}_4$ SSEs. b,c) 2D diffraction patterns from $g\text{-Li}_{3.2}\text{P}_{0.8}\text{Sn}_{0.2}\text{S}_4$ (b) and $gc\text{-Li}_{3.2}\text{P}_{0.8}\text{Sn}_{0.2}\text{S}_4$ SSEs (c), which were recorded on a Pilatus 1M detector at the VESPERs beamline. d) Raman spectra of $gc\text{-Li}_{3.2}\text{P}_{0.8}\text{Sn}_{0.2}\text{S}_4$ SSEs compared with $gc\text{-Li}_3\text{PS}_4$ and crystallized Li_4SnS_4 SSEs. e) Rietveld refinement patterns for $gc\text{-Li}_{3.2}\text{P}_{0.8}\text{Sn}_{0.2}\text{S}_4$ SSEs with an inset image of the unit cell. f) ^{119}Sn and g) ^{31}P MAS NMR spectra of $gc\text{-Li}_{3.2}\text{P}_{0.8}\text{Sn}_{0.2}\text{S}_4$ (red) and $g\text{-Li}_{3.2}\text{P}_{0.8}\text{Sn}_{0.2}\text{S}_4$ (black) SSEs. h) Deconvolution of the ^{31}P MAS NMR spectrum of $gc\text{-Li}_{3.2}\text{P}_{0.8}\text{Sn}_{0.2}\text{S}_4$ SSEs. Spinning sidebands are marked with asterisks.

occupation ratio of 17%, which is very close to the designed substitution content of 20% (Table S3, Supporting Information). The inserted schematic diagram in Figure 1e shows the crystal structure of $\text{Li}_{3.2}\text{P}_{0.8}\text{Sn}_{0.2}\text{S}_4$, which is mainly composed of Li cations and $(\text{P}/\text{Sn})\text{S}_4$ anions. The Sn-substituted P atom (P/Sn) is located in the coordination center to bond with surrounding S atoms to form tetrahedral $(\text{P}/\text{Sn})\text{S}_4$ anions. The isolated $(\text{P}/\text{Sn})\text{S}_4$ tetrahedra are distributed in layers perpendicular to the a -axis kept apart by the Li_6 octahedrons and Li_4S_4 tetrahedra (Li–S bonding is omitted to facilitate the observation of the incorporated Sn).

^{119}Sn and ^{31}P MAS NMR measurements were further carried out to obtain detailed structural and compositional information for the $g\text{-Li}_{3.2}\text{P}_{0.8}\text{Sn}_{0.2}\text{S}_4$ and $gc\text{-Li}_{3.2}\text{P}_{0.8}\text{Sn}_{0.2}\text{S}_4$ SSEs. ^{119}Sn and ^{31}P MAS spectra of both the glass and glass-ceramic samples exhibit a single resonance. However, the ^{119}Sn and ^{31}P peaks in the glass-ceramic sample are sharper and more intense compared to those of the glass sample, suggesting significantly enhanced crystallinity with more ordered Sn and P local structures.^[35] As displayed in Figure 1f, ^{119}Sn resonance signals appear at 55.0 and 67.8 ppm for the glass and glass-ceramic samples, respectively. These chemical shift

values are in the range of reported values for SnS_4 tetrahedra in various tin sulfides.^[21,36] The confirmed tetrahedral geometry around Sn is consistent with the above Raman analysis for the gc- $\text{Li}_{3.2}\text{P}_{0.8}\text{Sn}_{0.2}\text{S}_4$ SSEs. ^{31}P MAS spectrum of the g- $\text{Li}_{3.2}\text{P}_{0.8}\text{Sn}_{0.2}\text{S}_4$ SSEs (Figure 1g) exhibits two signals: a very weak peak at 105.6 ppm and a strong peak at 83.2 ppm. The former is assigned to P_2S_6 units and the later to PS_4 tetrahedra, which agrees well with previously reported results in the glass Li_3PS_4 .^[35] Upon annealing, the small peak due to P_2S_6 units disappeared completely in the spectrum of the gc- $\text{Li}_{3.2}\text{P}_{0.8}\text{Sn}_{0.2}\text{S}_4$ SSEs, while the characteristic peak of PS_4 tetrahedra moved to a higher chemical shift (871 ppm) and becomes more prominent. A careful inspection of the ^{31}P MAS spectrum of the glass-ceramic sample reveals that the 871 ppm peak has a weak shoulder appearing on the low-frequency side of the main peak. The deconvoluted spectrum shown in Figure 1h illustrates that the weak shoulder represents a signal positioned at 83.2 ppm coinciding with the amorphous peak in the glass sample. Therefore, the 83.2 and 871 ppm resonances in the deconvoluted spectrum are assigned to the amorphous and crystalline components, respectively. On the basis of the peak area of each signal derived from spectral integration, the amorphous content in the glass-ceramic sample is estimated at 12%. To the best of our knowledge, this is the first time that the amorphous and crystalline contents are estimated in glass-ceramic SSEs.

The structural and compositional analysis confirms that the lower-valence Sn (IV) partially replaces P (V) to form a new gc- $\text{Li}_{3.2}\text{P}_{0.8}\text{Sn}_{0.2}\text{S}_4$ SSE. The quantification of the amorphous and crystallized parts in the glass-ceramic SSE is performed as well. The compensatory Li^+ ion concentration and enlarged unit cell

embedded in the amorphous matrix are achieved by the Sn substitution, which are favorable toward increasing the Li^+ transport and ionic conductivity. More importantly, the Sn–S bond is capable of improving air-stability. In addition, it is expected that a Li–Sn alloy will form at the Li/gc- $\text{Li}_{3.2}\text{P}_{0.8}\text{Sn}_{0.2}\text{S}_4$ interface, which can regulate the uniform Li deposition and enable high-performance ASSLMs at RT.

Electrochemical impedance spectroscopy (EIS) measurements were carried out to derive the Arrhenius plot of the prepared gc- $\text{Li}_{3.2}\text{P}_{0.8}\text{Sn}_{0.2}\text{S}_4$ SSEs. As shown in Figure 2a, the ionic conductivity (σ) of gc- $\text{Li}_{3.2}\text{P}_{0.8}\text{Sn}_{0.2}\text{S}_4$ reaches $1.21 \times 10^{-3} \text{ S cm}^{-1}$ at 25 °C, showing a 6.2-times increase for gc- Li_3PS_4 ($1.94 \times 10^{-4} \text{ S cm}^{-1}$) SSEs, and a 2.5-times increase for g- $\text{Li}_{3.2}\text{P}_{0.8}\text{Sn}_{0.2}\text{S}_4$ ($4.79 \times 10^{-4} \text{ S cm}^{-1}$). The σ of gc- $\text{Li}_{3.2}\text{P}_{0.8}\text{Sn}_{0.2}\text{S}_4$ is among the highest in all reported SSEs based on the ionic-conductive phase of $\beta\text{-Li}_3\text{PS}_4$, and is comparable to the well crystallized Li Argyrodites ($\text{Li}_6\text{PS}_5\text{Cl}$ and $\text{Li}_6\text{PS}_5\text{Br}$).^[6] And considering the ultralow electronic conductivity ($2.83 \times 10^{-9} \text{ S cm}^{-1}$) measured by chronoamperometry (CA) method (Figure S5, Supporting Information), our gc- $\text{Li}_{3.2}\text{P}_{0.8}\text{Sn}_{0.2}\text{S}_4$ SSEs can be expected to be used directly as a single electrolyte layer for ASSLMs. The activation energy (E_a) of prepared SSEs is deduced from the slope of the Arrhenius plots. It is found that the incorporation of Sn effectively reduces the obstacles and promotes Li^+ ion transport. Even in the glass state of g- $\text{Li}_{3.2}\text{P}_{0.8}\text{Sn}_{0.2}\text{S}_4$, the derived E_a is only 0.363 eV, which is lower than that of gc- Li_3PS_4 (0.381 eV), and the E_a of the partially crystallized gc- $\text{Li}_{3.2}\text{P}_{0.8}\text{Sn}_{0.2}\text{S}_4$ is further decreased to 0.311 eV. To further analyze the Li^+ ion dynamics of the gc- $\text{Li}_{3.2}\text{P}_{0.8}\text{Sn}_{0.2}\text{S}_4$ SSEs, ^7Li SS-NMR experiments were conducted. ^7Li spin–lattice relaxation (SLR) rates ($1/T_1$) were measured as a function of temperature (T). As shown in Figure 2b, the

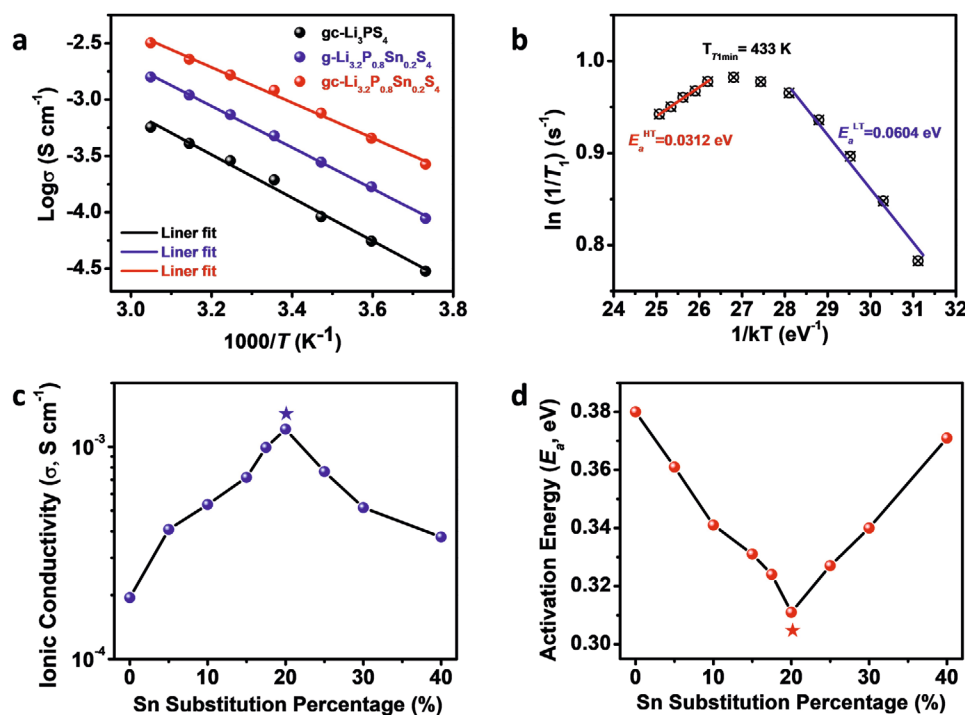


Figure 2. Li^+ ion dynamics in gc- $\text{Li}_{3.2}\text{P}_{0.8}\text{Sn}_{0.2}\text{S}_4$ SSEs. a) Arrhenius plots of gc- $\text{Li}_{3.2}\text{P}_{0.8}\text{Sn}_{0.2}\text{S}_4$, g- $\text{Li}_{3.2}\text{P}_{0.8}\text{Sn}_{0.2}\text{S}_4$, and gc- Li_3PS_4 SSEs derived from the EIS measurements in a range of -5 to 55 °C. b) Temperature-dependent ^7Li SLR rates measured in the laboratory frame for gc- $\text{Li}_{3.2}\text{P}_{0.8}\text{Sn}_{0.2}\text{S}_4$ SSEs. c) Ionic conductivities and d) activation energies of gc- $\text{Li}_{3+x}\text{P}_{1-x}\text{Sn}_x\text{S}_4$ ($x = 0, 0.05, 0.1, 0.15, 0.175, 0.2, 0.25, 0.3,$ and 0.4) SSEs.

$\ln(1/T_1)$ versus T plot shows a maximum at the temperature of 433 K (i.e., $T_{T\min} = 433$ K) for gc-Li_{3.2}P_{0.8}Sn_{0.2}S₄ SSEs. The jump rate of Li⁺ ions in both the high-temperature and low-temperature regimes fulfill the Arrhenius equation, which correspond to the Li⁺ ion transport in long-range and short-range, respectively.^[37] In this way, the activation energy for long-range (E_a^{LT}) and short-range (E_a^{ST}) transport can be deduced from the slopes at 0.0312 and 0.0604 eV, respectively. It is not unreasonable that the E_a measured via ⁷Li SS-NMR is lower than that derived from the EIS measurement, because the NMR results truly reflect the intrinsic Li⁺ ion dynamics without being influenced by effects such as grain boundaries.^[38] For gc-Li₃PS₄ SSEs, the maximum of $\ln(1/T_1)$ occurs at 453 K (Figure S6, Supporting Information). The improved turnover temperature (compared to 433 K for gc-Li_{3.2}P_{0.8}Sn_{0.2}S₄) suggests that Li⁺ ion hopping becomes more difficult in the gc-Li₃PS₄ SSEs without Sn incorporation.^[37,38] This is further reflected by the higher activation energy (E_a^{LT}) of 0.158 eV for the gc-Li₃PS₄ SSEs.

Both EIS and NMR results confirm that the new gc-Li_{3.2}P_{0.8}Sn_{0.2}S₄ SSEs possess a favorable structure for Li⁺ ion transport. Partial replacement of P with Sn expands the unit cell and improves the Li⁺ ion concentration, which dominate the main causes of the significantly improved Li⁺ ion transport capability. Moreover, the unique glass-ceramic structure can maximize the σ of the metastable β -phase superionic conductor (Li_{3.2}P_{0.8}Sn_{0.2}S₄) at RT. In addition, we have also investigated the influence of Sn content on the σ and E_a by preparing a series of gc-Li_{3+x}P_{1-x}Sn_xS₄ SSEs, where x is equal to 0, 0.05, 0.1, 0.15, 0.2, 0.25, 0.3, and 0.4. The trends of the σ and E_a evolution along with the Sn percentage are displayed in Figure 2c,d, respectively. 20% ($x = 0.2$) was found to be the

optimized ratio, where the σ is the highest and E_a is the lowest comparing to other compositions. When $x < 0.2$, although the expanded unit cell and increased Li⁺ ion concentration do lead to an improved σ and reduced E_a , the improvement is not sufficient. Nevertheless, the σ appears to drop and the E_a increases when $x > 0.2$. This might be related to the lattice tolerance of the β -phase crystal structure, which also appeared in other sulfide SSEs built based on the PS₄³⁻ blocks.^[23,24] In other words, once the incorporated percentage of Sn reaches a maximum while maintaining the orthorhombic phase, any further increase in the ratio may cause the collapse/distortion of this target phase or the generation of impurities.^[39]

To examine whether the gc-Li_{3.2}P_{0.8}Sn_{0.2}S₄ SSEs can satisfy the processing requirements of dry room manufacturing for practical applications, we studied its resistance toward air with 5% humidity. After exposing the gc-Li_{3.2}P_{0.8}Sn_{0.2}S₄ SSEs to air with 5% humidity overnight, it was found that the crystal structure maintains unchanged (Figure 3a). EIS measurements for the 5% humidity air-exposed gc-Li_{3.2}P_{0.8}Sn_{0.2}S₄ SSEs show negligible changes of σ (1.03×10^{-3} S cm⁻¹ at RT) and E_a (0.320 eV), as displayed in Figure 3b. For comparison, the same exposure experiment was conducted on the gc-Li₃PS₄ SSEs. Relative intensity changes of the characteristic diffraction peaks and formation of impure phases (Figure S7, Supporting Information) suggest that structural evolution and damage have occurred to the gc-Li₃PS₄ SSEs after exposure to air with 5% humidity overnight. Accordingly, a significant decline of σ (2.53×10^{-5} S cm⁻¹ at RT) and increase of E_a (0.456 eV) appear for the 5% humidity air-exposed gc-Li₃PS₄ SSEs (Figure 3c). Furthermore, as shown in Figure S8 (Supporting Information), we tried exposing our

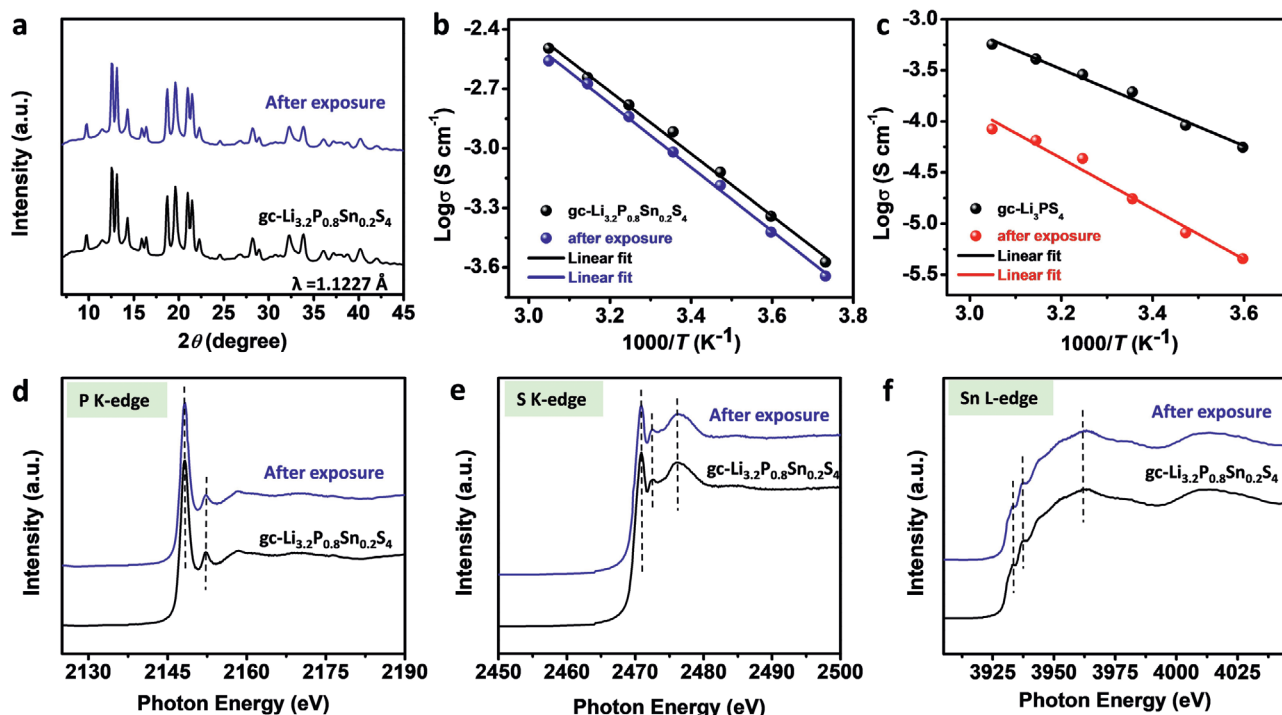


Figure 3. Characterization of the air-stability of the gc-Li_{3.2}P_{0.8}Sn_{0.2}S₄ SSEs. a) Synchrotron-based XRD patterns of the gc-Li_{3.2}P_{0.8}Sn_{0.2}S₄ SSEs before and after exposure to air with 5% humidity. b,c) Arrhenius plots of the gc-Li_{3.2}P_{0.8}Sn_{0.2}S₄ SSEs (b) and gc-Li₃PS₄ SSEs (c) before and after exposure to air with 5% humidity. d–f) XANES of P K-edge (d), S-K-edge (e), and Sn L₃-edge (f) of the gc-Li_{3.2}P_{0.8}Sn_{0.2}S₄ SSEs before and after exposure to air with 5% humidity.

gc-Li_{3.2}P_{0.8}Sn_{0.2}S₄ SSEs to the air with other humidity values (1–3%, 10%, and 20%) and found that 5% humidity is the upper limit if an ionic conductivity of 10⁻³ S cm⁻¹ is considered as an essential indicator for battery applications.

XANES analysis was further conducted to confirm the structure stability of gc-Li_{3.2}P_{0.8}Sn_{0.2}S₄ SSEs after exposure to the air with 5% humidity. As displayed in Figure 3d–f, the featured peaks and spectral shapes of the P K-edge, S K-edge, and Sn L₃-edge are consistent with those in the pristine gc-Li_{3.2}P_{0.8}Sn_{0.2}S₄ SSEs, and are in agreement with previously reported features.^[40,41] While decreased peak (whiteline) intensity and peak-energy-position shift of both P K-edge and S K-edge can be observed in the gc-Li₃PS₄ SSEs after exposure to the same ambient environment, illustrating the structural decomposition due to the exposure (Figure S9, Supporting Information). The good air-stability of gc-Li_{3.2}P_{0.8}Sn_{0.2}S₄ SSEs is ascribed to the strong binding energy of Sn–S, which is difficult to break via reaction with H₂O in the moist air. This leads to a stabilized (P/Sn)S₄ tetrahedron, as well as keeping the glass

part steady when exposed to 5% humidity air. Therefore, gc-Li_{3.2}P_{0.8}Sn_{0.2}S₄ SSEs have the potential to be used in the dry room for large-scale processing.

Symmetric cells of Li//gc-Li_{3.2}P_{0.8}Sn_{0.2}S₄//Li were assembled to evaluate the Li metal compatibility. As shown in Figure 4a, the symmetric cell presents a long cycle with stable Li plating/stripping for over 600 h at a current density of 0.1 mA cm⁻² and a cutoff capacity of 0.1 mAh cm⁻², prolonging the lifetime by 4 times compared to the Li//gc-Li₃PS₄//Li symmetric cell (Figure S10, Supporting Information). Close observations of the polarization curves (Figure 4a-1,2, and 3) suggest that the Li//gc-Li_{3.2}P_{0.8}Sn_{0.2}S₄//Li cell experienced an activation process in the initial 300 h. The overpotential increases from ≈25 to ≈150 mV in this period, which corresponds to the formation of a stabilized Li/gc-Li_{3.2}P_{0.8}Sn_{0.2}S₄ interface. The nearly unchanged overpotential after 300 h proves that the in-situ formation of the interface is self-terminating due to the deficiency of electron/electron providers, and this stabilized interface can support a smooth Li plating/stripping process subsequently.

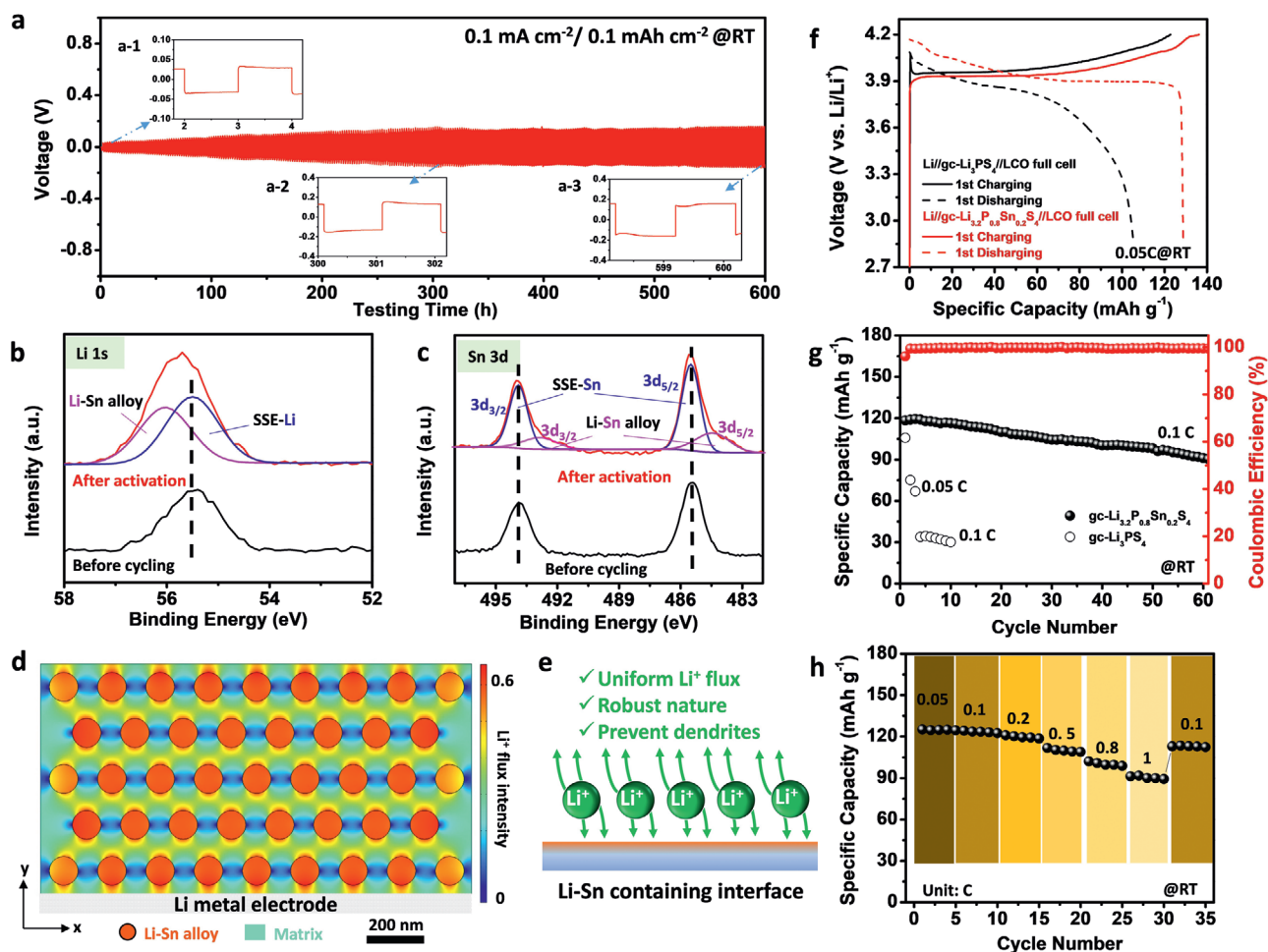


Figure 4. a) Polarization curve of the Li//gc-Li_{3.2}P_{0.8}Sn_{0.2}S₄//Li symmetric cell tested at 0.1 mA cm⁻²/0.1 mAh cm⁻² and RT. a-1, 2, and 3) Magnified regions of the polarization curves in (a). b) Li 1s and c) Sn 3d XPS spectra of the interfacial compositions between Li and gc-Li_{3.2}P_{0.8}Sn_{0.2}S₄ SSEs compared to the pristine Li_{3.2}P_{0.8}Sn_{0.2}S₄ SSEs before cycling. d) Simulation results of Li⁺ flux distribution at the interface formulated by the finite element method. e) Schematic diagram of the working mechanism of the gc-Li_{3.2}P_{0.8}Sn_{0.2}S₄ derived Li anode interface enabling high-performance ASLMBs. f) Charging and discharging curves of the Li//gc-Li_{3.2}P_{0.8}Sn_{0.2}S₄//LCO full cell compared to the Li//gc-Li₃PS₄//LCO full cell. g) Cycling stability of Li//gc-Li_{3.2}P_{0.8}Sn_{0.2}S₄//LCO at 0.1 C and RT. h) Rate capability of Li//gc-Li_{3.2}P_{0.8}Sn_{0.2}S₄//LCO at RT.

The cycling time-resolved EIS plots for the symmetric cell are displayed correspondingly in Figure S11 (Supporting Information). The change of the impedance of the in-situ formed Li/gc-Li_{3.2}P_{0.8}Sn_{0.2}S₄ interface agrees well with the evolution of overpotential as discussed above. SEM images of the Li metal surface after cycling against gc-Li_{3.2}P_{0.8}Sn_{0.2}S₄ for 300 h are presented in Figure S12 (Supporting Information). It is found that the surface is very smooth, consisting of nanosized domains. X-ray photoelectron spectroscopy (XPS) was used to analyze the chemical composition of the activated Li/gc-Li_{3.2}P_{0.8}Sn_{0.2}S₄ interface. XPS spectra of Li 1s and Sn 3d at the SSE pellet surface are displayed in Figure 4b,c, respectively. The peak at 55.5 eV is assigned to the Li (+1) in the gc-Li_{3.2}P_{0.8}Sn_{0.2}S₄ SSEs. A new Li 1s peak located at 56.1 eV can be observed after the activation process. Accordingly, Sn is observed in a reduced state based on the Sn 3d spectrum. The main peaks assigned to the electrolyte are located at 493.9 and 485.5 eV corresponding to the 3d_{3/2} and 3d_{5/2}, respectively. One additional pair of 3d peaks is seen to emerge at 492.9 and 484.5 eV, indicating some reduction of Sn.^[42,43] The generation of the new peaks in Li 1s and Sn 3d regions suggest the formation of Li–Sn alloys during the activation process.^[42]

Indeed, Li–Sn alloy has been used as a functional interlayer to improve the interfacial property between Li metal and organic liquid or Garnet-type electrolytes,^[42–45] but it is rarely reported as an effective component to mitigate the thermodynamically unstable interface between Li metal and sulfide SSEs. It was generally believed that the electronically conductive Li–Sn alloy would boost the detrimental side reactions, thus reducing cycling performance.^[46] However, we propose that Li–Sn alloys can still regulate the Li deposition at the interface of Li/sulfide SSEs, once a balance between the undesired effect of electronic conductivity and the positive Li plating/stripping nucleation derived from Li–Sn alloys is achieved. Incorporating Sn in gc-Li_{3.2}P_{0.8}Sn_{0.2}S₄ SSEs rather than direct application as an interlayer is demonstrated as an excellent example to achieve this balance due to the in-situ formation of the electronically conductive Li–Sn alloy as well as insulating Li₂S and Li₃P interfacial products (Figure S13, Supporting Information) with a homogeneous distribution.^[47] SEM with EDS analysis (Figure S14, Supporting Information) for the cycled Li/SSE interface verifies the uniform dispersion of nanosized Li–Sn alloys and other insulating interfacial species.^[42] We further developed a numerical simulation with the finite element method (FEM) to emulate the distribution of Li⁺ flux at the interface. As shown in Figure 4d, in the physical model consisting of well-dispersed Li–Sn alloys and matrix (Li₂S and Li₃P), the intensity of Li⁺ flux at the sites of Li–Sn alloys is obviously higher than that in the matrix. The high-intensity sites of Li⁺ flux centered with Li–Sn alloys are distributed homogeneously and connected with each other, constructing a high-speed transport network to keep the uniformity of Li⁺ flux through the entire interface and toward the Li metal electrode. The values of Li⁺ flux along the diagonal of the rectangular model are recorded against *x* and *y* axes (Figure S15, Supporting Information), which are considered representative to witness the high Li⁺ flux around Li–Sn alloys comparing to the poor Li⁺ flux through the matrix. So far, we can reveal the working mechanism of the Li–Sn alloy-containing interface for the sulfide-based ASSLMBs as

schematically shown in Figure 4e. The Li–Sn alloy and other insulating compounds (Li₃P and Li₂S) constitute a smooth Li anode interface. The uniformly embedded nanoscale Li–Sn alloy is beneficial to provide uniform Li⁺ flux and regulate stable Li plating/stripping (preventing Li dendrites),^[44,45] while the insulating interfacial products can effectively prevent further parasitic side reactions (robust nature).

Full cells were assembled to investigate the application potential of gc-Li_{3.2}P_{0.8}Sn_{0.2}S₄ SSEs. As shown in the schematic diagram of the full-cell configuration (Figure S16, Supporting Information), the gc-Li_{3.2}P_{0.8}Sn_{0.2}S₄ SSE is employed as the electrolyte layer to separate Li metal anode and LiCoO₂/Li₃InCl₆ (LCO/LIC) cathode. The LCO loading reaches 8.9 mg cm⁻². LCO/LIC cathode composites are used due to the highly stable cathode interface.^[48] The Li/gc-Li_{3.2}P_{0.8}Sn_{0.2}S₄/LCO full cell possesses excellent charging/discharging behavior at a current density of 0.05 C (1 C corresponds to 140 mA g⁻¹), as demonstrated in Figure 4f. In contrast, the full cell using gc-Li₃PS₄ as the electrolyte layer (Li/gc-Li₃PS₄/LCO) shows a large polarization and poor reversibility, which is an integrative reflection of the low σ and the unstable Li/gc-Li₃PS₄ interface. The ASSLMBs (Li/gc-Li_{3.2}P_{0.8}Sn_{0.2}S₄/LCO) exhibit good durability at 0.1 C (Figure 4g). Specifically, the initial Coulombic efficiency reaches 96.18%, and the average value is 99.8% for the following 60 cycles. A reversible specific capacity of 118.4 mAh g⁻¹ is achieved for the first cycle, and maintains 91.1 mAh g⁻¹ after 60 cycles, showing a retention of 77%. Comparatively, the full battery using gc-Li₃PS₄ as the electrolyte layer shows a fast capacity decay at 0.05 C and a limited reversible capacity of \approx 30 mAh g⁻¹ at 0.1 C. The rate performance of the Li/gc-Li_{3.2}P_{0.8}Sn_{0.2}S₄/LCO full cell was examined by elevating the discharging current densities, while keeping the charging current at 0.05 C to ensure complete delithiation of the cathode materials. As shown in Figure 4h, the reversible capacity is 124.7 mAh g⁻¹ at the initial current density of 0.05 C. Along with the current density is increased, although the polarization becomes gradually increased (Figure S17, Supporting Information), a capacity retention of 91.0 mAh g⁻¹ can still be achieved under a high rate of 1 C. Afterward, the capacity recovers to 113.0 mAh g⁻¹ when the current rate is reverted to 0.1 C. Compared to other reported results, the cell performance using gc-Li_{3.2}P_{0.8}Sn_{0.2}S₄ SSE is among the best without any interlayer protection or Li metal modifications (Table S4, Supporting Information).

In summary, an advanced glass-ceramic sulfide-based SSE (gc-Li_{3.2}P_{0.8}Sn_{0.2}S₄) has been developed to satisfy all the requirements for the development of practical ASSLMBs. Table S5 (Supporting Information) summarizes the basic physicochemical properties of gc-Li_{3.2}P_{0.8}Sn_{0.2}S₄ SSEs compared with other representative sulfide-based SSEs. The ionic conductivity can reach as high as 1.21×10^{-3} S cm⁻¹ at RT, which is one of the highest values among all the reported SSEs based on orthorhombic β -Li₃PS₄. Selective Sn (IV) substitution for P (V) is verified to enlarge the unit cell and induce increased Li⁺ ion concentration to enhance the ionic conductivity. The amorphous content is estimated at 12% via analysis of the ³¹P MAS NMR spectrum of gc-Li_{3.2}P_{0.8}Sn_{0.2}S₄ SSEs. Excellent air-stability in a conventional dry-room level atmosphere (5% air humidity) is also obtained via the construction of strong Sn–S bonds and

stabilized (P/Sn)₄ tetrahedrons in the gc-Li_{3.2}P_{0.8}Sn_{0.2}S₄ SSEs. In addition, Sn substitution triggers the formation of Li–Sn alloys at the anode interface. It is verified by the FEM-based numerical simulation that interfacial Li–Sn alloys can regulate stable Li plating/stripping, thus leading to improved Li metal compatibility. As a final result, the gc-Li_{3.2}P_{0.8}Sn_{0.2}S₄ SSE can be employed as a single electrolyte layer to enable ASSLMs with excellent electrochemical performance, presenting great opportunity for industrial application.

Supporting Information

Supporting Information is available from the Wiley Online Library or from the author.

Acknowledgements

F.Z., S.H.A., and K.A. contributed equally to this work. This research was supported by the Natural Sciences and Engineering Research Council of Canada (NSERC), the Canada Research Chair Program (CRC), the Canada Foundation for Innovation (CFI), Ontario Research Foundation (ORF), China Automotive Battery Research Institute Co., Ltd., Glatat Solid-State Battery Inc., and the University of Western Ontario (UWO). The synchrotron research was performed at the Canadian Light Source, which is supported by the Canada Foundation for Innovation (CFI), the Natural Sciences and Engineering Research Council (NSERC), the National Research Council (NRC), the Canadian Institutes of Health Research (CIHR), the Government of Saskatchewan, and the University of Saskatchewan. The authors gratefully acknowledge Dr. Mathew Willans for his kind help on the test and analysis of NMR at J. B. Stothers NMR facility in the University of Western Ontario. The authors also appreciate the technical support of Dr. Qunfeng Xiao and Dr. Mohsen Shakourithe at the SXRMB beamline of Canadian Light Source.

Conflict of Interest

The authors declare no conflict of interest.

Keywords

air-stability, all-solid-state Li metal batteries, glass-ceramic electrolytes, Li metal compatibility, superionic conductors

Received: September 27, 2020

Revised: November 19, 2020

Published online: January 20, 2021

- [1] P. Albertus, S. Babinec, S. Litzelman, A. Newman, *Nat. Energy* **2018**, 3, 16.
- [2] Q. Zhao, S. Stalin, C.-Z. Zhao, L. A. Archer, *Nat. Rev. Mater.* **2020**, 5, 229.
- [3] G. Cui, *Matter* **2020**, 2, 805.
- [4] W. Zhao, J. Yi, P. He, H. Zhou, *Electrochem. Energy Rev.* **2019**, 2, 574.
- [5] R. Chen, Q. Li, X. Yu, L. Chen, H. Li, *Chem. Rev.* **2019**, 120, 6820.
- [6] Q. Zhang, D. Cao, Y. Ma, A. Natan, P. Aurora, H. Zhu, *Adv. Mater.* **2019**, 31, 1901131.
- [7] H. Lee, P. Oh, J. Kim, H. Cha, S. Chae, S. Lee, J. Cho, *Adv. Mater.* **2019**, 31, 1900376.
- [8] A. Hayashi, K. Noi, A. Sakuda, M. Tatsumisago, *Nat. Commun.* **2012**, 3, 856.
- [9] A. Hayashi, M. Tatsumisago, *Electron. Mater. Lett.* **2012**, 8, 199.
- [10] Z. Zhang, Y. Shao, B. Lotsch, Y.-S. Hu, H. Li, J. Janek, L. F. Nazar, C.-W. Nan, J. Maier, M. Armand, L. Chen, *Energy Environ. Sci.* **2018**, 11, 1945.
- [11] K. Homma, M. Yonemura, T. Kobayashi, M. Nagao, M. Hirayama, R. Kanno, *Solid State Ionics* **2011**, 182, 53.
- [12] H. Tsukasaki, S. Mori, H. Morimoto, A. Hayashi, M. Tatsumisago, *Sci. Rep.* **2017**, 7, 4142.
- [13] F. Mizuno, A. Hayashi, K. Tadanaga, M. Tatsumisago, *Adv. Mater.* **2005**, 17, 918.
- [14] Y. Seino, T. Ota, K. Takada, A. Hayashi, M. Tatsumisago, *Energy Environ. Sci.* **2014**, 7, 627.
- [15] Y. Xiao, Y. Wang, S.-H. Bo, J. C. Kim, L. J. Miara, G. Ceder, *Nat. Rev. Mater.* **2019**, 5, 105.
- [16] H. Muramatsu, A. Hayashi, T. Ohtomo, S. Hama, M. Tatsumisago, *Solid State Ionics* **2011**, 182, 116.
- [17] Y. Zhu, X. He, Y. Mo, *ACS Appl. Mater. Interfaces* **2015**, 7, 23685.
- [18] M. Nagao, A. Hayashi, M. Tatsumisago, T. Kanetsuku, T. Tsuda, S. Kuwabata, *Phys. Chem. Chem. Phys.* **2013**, 15, 18600.
- [19] Y. Zhang, T.-T. Zuo, J. Popovic, K. Lim, Y.-X. Yin, J. Maier, Y.-G. Guo, *Mater. Today* **2020**, 33, 56.
- [20] J. A. Brant, D. M. Massi, N. A. W. Holzwarth, J. H. MacNeil, A. P. Douvalis, T. Bakas, S. W. Martin, M. D. Gross, J. A. Aitken, *Chem. Mater.* **2014**, 27, 189.
- [21] T. Kaib, S. Haddadpour, M. Kapitein, P. Bron, C. Schröder, H. Eckert, B. Roling, S. Dehnen, *Chem. Mater.* **2012**, 24, 2211.
- [22] G. Sahu, Z. Lin, J. Li, Z. Liu, N. Dudney, C. Liang, *Energy Environ. Sci.* **2014**, 7, 1053.
- [23] F. P. Zhao, J. W. Liang, C. Yu, Q. Sun, X. N. Li, K. Adair, C. H. Wang, Y. Zhao, S. M. Zhang, W. H. Li, S. X. Deng, R. Y. Li, Y. N. Huang, H. Huang, L. Zhang, S. Q. Zhao, S. G. Lu, X. L. Sun, *Adv. Energy Mater.* **2020**, 10, 1903422.
- [24] J. Liang, N. Chen, X. Li, X. Li, K. R. Adair, J. Li, C. Wang, C. Yu, M. Norouzi Banis, L. Zhang, S. Zhao, S. Lu, H. Huang, R. Li, Y. Huang, X. Sun, *Chem. Mater.* **2020**, 32, 2664.
- [25] G. Z. Liu, D. J. Xie, X. L. Wang, X. Y. Yao, S. J. Chen, R. J. Xiao, H. Li, X. X. Xu, *Energy Storage Mater.* **2019**, 17, 266.
- [26] H. Kwak, K. H. Park, D. Han, K.-W. Nam, H. Kim, Y. S. Jung, *J. Power Sources* **2020**, 446, 227338.
- [27] Y. Gao, D. W. Wang, Y. G. C. Li, Z. X. Yu, T. E. Mallouk, D. H. Wang, *Angew. Chem., Int. Ed.* **2018**, 57, 13608.
- [28] C. Wang, Y. Zhao, Q. Sun, X. Li, Y. Liu, J. Liang, X. Li, X. Lin, R. Li, K. R. Adair, L. Zhang, R. Yang, S. Lu, X. Sun, *Nano Energy* **2018**, 53, 168.
- [29] R. Xu, F. Han, X. Ji, X. Fan, J. Tu, C. Wang, *Nano Energy* **2018**, 53, 958.
- [30] X. Fan, X. Ji, F. Han, J. Yue, J. Chen, L. Chen, T. Deng, J. Jiang, C. Wang, *Sci. Adv.* **2018**, 4, 12.
- [31] F. Zhao, Q. Sun, C. Yu, S. Zhang, K. Adair, S. Wang, Y. Liu, Y. Zhao, J. Liang, C. Wang, X. Li, X. Li, W. Xia, R. Li, H. Huang, L. Zhang, S. Zhao, S. Lu, X. Sun, *ACS Energy Lett.* **2020**, 5, 1035.
- [32] F. Han, J. Yue, X. Zhu, C. Wang, *Adv. Energy Mater.* **2018**, 8, 1703644.
- [33] K. Kanazawa, S. Yubuchi, C. Hotehama, M. Otoyama, S. Shimono, H. Ishibashi, Y. Kubota, A. Sakuda, A. Hayashi, M. Tatsumisago, *Inorg. Chem.* **2018**, 57, 9925.
- [34] S. Yubuchi, S. Teragawa, K. Aso, K. Tadanaga, A. Hayashi, M. Tatsumisago, *J. Power Sources* **2015**, 293, 941.
- [35] H. Stoffer, T. Zinkevich, M. Yavuz, A. L. Hansen, M. Knapp, J. Bednarcik, S. Randau, F. H. Richter, J. Janek, H. Ehrenberg, S. Indris, *J. Phys. Chem. C* **2019**, 123, 10280.
- [36] C. Mundus, G. Taillades, A. Pradel, M. Ribes, *Solid State Nucl. Magn. Reson.* **1996**, 7, 141.
- [37] C. Yu, Y. Li, M. Willans, Y. Zhao, K. R. Adair, F. P. Zhao, W. H. Li, S. X. Deng, J. W. Liang, M. N. Banis, R. Y. Li, H. Huang, L. Zhang, R. Yang, S. G. Lu, Y. N. Huang, X. L. Sun, *Nano Energy* **2020**, 69, 104396.

- [38] S. Ganapathy, C. Yu, E. R. H. van Eck, M. Wagemaker, *ACS Energy Lett.* **2019**, *4*, 1092.
- [39] W. Travis, E. N. K. Glover, H. Bronstein, D. O. Scanlon, R. G. Palgrave, *Chem. Sci.* **2016**, *7*, 4548.
- [40] T. Hakari, M. Deguchi, K. Mitsuhashi, T. Ohta, K. Saita, Y. Orikasa, Y. Uchimoto, Y. Kowada, A. Hayashi, M. Tatsumisago, *Chem. Mater.* **2017**, *29*, 4768.
- [41] X. L. Zheng, P. De Luna, F. P. G. de Arquer, B. Zhang, N. Becknell, M. B. Ross, Y. F. Li, M. N. Banis, Y. Z. Li, M. Liu, O. Voznyy, C. T. Dinh, T. T. Zhuang, P. Stadler, Y. Cui, X. W. Du, P. D. Yang, E. H. Sargent, *Joule* **2017**, *1*, 794.
- [42] M. T. Wan, S. J. Kang, L. Wang, H. W. Lee, G. W. Zheng, Y. Cui, Y. M. Sun, *Nat. Commun.* **2020**, *11*, 829.
- [43] K. Shi, Z. Wan, L. Yang, Y. Zhang, Y. Huang, S. Su, H. Xia, K. Jiang, L. Shen, Y. Hu, S. Zhang, J. Yu, F. Ren, Y. B. He, F. Kang, *Angew. Chem., Int. Ed.* **2020**, *132*, 11882.
- [44] Z. Y. Tu, S. Choudhury, M. J. Zachman, S. Y. Wei, K. H. Zhang, L. F. Kourkoutis, L. A. Archer, *Nat. Energy* **2018**, *3*, 310.
- [45] M. He, Z. Cui, C. Chen, Y. Li, X. Guo, *J. Mater. Chem. A* **2018**, *6*, 11463.
- [46] S. Wenzel, T. Leichtweiss, D. Krüger, J. Sann, J. Janek, *Solid State Ionics* **2015**, *278*, 98.
- [47] A. Kato, H. Kowada, M. Deguchi, C. Hotehama, A. Hayashi, M. Tatsumisago, *Solid State Ionics* **2018**, *322*, 1.
- [48] X. Li, J. Liang, J. Luo, M. Norouzi Banis, C. Wang, W. Li, S. Deng, C. Yu, F. Zhao, Y. Hu, T.-K. Sham, L. Zhang, S. Zhao, S. Lu, H. Huang, R. Li, K. R. Adair, X. Sun, *Energy Environ. Sci.* **2019**, *12*, 2665.